



Statistical analysis of surface urban heat island intensity variations: A case study of Babol city, Iran

Qihao Weng, Mohammad Karimi Firozjaei, Amir Sedighi, Majid Kiavarz & Seyed Kazem Alavipanah

To cite this article: Qihao Weng, Mohammad Karimi Firozjaei, Amir Sedighi, Majid Kiavarz & Seyed Kazem Alavipanah (2019) Statistical analysis of surface urban heat island intensity variations: A case study of Babol city, Iran, GIScience & Remote Sensing, 56:4, 576-604, DOI: [10.1080/15481603.2018.1548080](https://doi.org/10.1080/15481603.2018.1548080)

To link to this article: <https://doi.org/10.1080/15481603.2018.1548080>



Published online: 19 Nov 2018.



Submit your article to this journal [↗](#)



Article views: 1777



View related articles [↗](#)






View Crossmark data [↗](#)



Citing articles: 33 View citing articles [↗](#)



Statistical analysis of surface urban heat island intensity variations: A case study of Babol city, Iran

Qihao Weng ^a, Mohammad Karimi Firozjaei ^b, Amir Sedighi ^b, Majid Kiavarz*^b
and Seyed Kazem Alavipanah^b

^aCenter for Urban and Environmental Chang, Department of Earth and Environmental Systems, Indiana State University, Terre Haute, IN, USA; ^bDepartment of Remote Sensing and GIS, Faculty of Geography, University of Tehran, Tehran, Iran

(Received 2 June 2018; accepted 5 November 2018)

The urban heat island is considered as one of the most important climate change phenomena in urban areas, which can result in remarkable negative effects on flora, concentration of pollutants, air quality, energy and water consumption, human health, ecological and economic impacts, and even on global warming. The variation analysis of the surface urban heat island intensity (SUHII) is important for understanding the effect of urbanization and urban planning. The objective of this study was to present a new strategy based on the Shannon's entropy and Pearson chi-square statistic to investigate the spatial and temporal variations of the SUHII. In this study, Landsat TM, ETM+, OLI and TIRS images, MODIS products, meteorological data, topographic and population maps of the Babol city, Iran, from 1985 to 2017, and air temperature data recorded by ground recorder devices in 2017 were used. First, Single-Channel algorithm was used to estimate land surface temperature (LST), and the maximum likelihood classifier was employed to classify Landsat images. Then, based on LST maps, surface urban heat island ratio index was employed to calculate the SUHII. Further, several statistical methods, such as the degree-of-freedom, degree-of-sprawl and degree-of-goodness, were used to analyse the SUHII variation along different geographic directions and in various time periods. Finally, correlation between various parameters such as air temperature, SUHII, population variation and degree-of-goodness index values were investigated. The results indicated that the SUHII value increased by 24% in Babol over different time periods. The correlation coefficient yielded 0.82 between the values of the difference between the mean air temperature of the urban and suburbs and the SUHII values for the geographic directions. Furthermore, the correlation coefficient between the population variation and the degree-of-goodness index values reached 0.8. The results suggested that the SUHII variation of Babol city had a high degree-of-freedom, high degree-of-sprawl and negative degree-of-goodness.

Keywords: Landsat imagery; surface urban heat island; spatio-temporal variations; statistical analysis; Babol city

1. Introduction

More than half of the world's population are living in cities (Shen et al. 2016), and some studies suggest that the percentage of urban population in total population will reach to 75% by 2050 (Sun and Zhao 2018). High-rate urbanization leads to increasing change of

*Corresponding author. Majid Kiavarz Email: kiavarzmajid@ut.ac.ir

This article has been republished with minor changes. These changes do not impact the academic content of the article.

natural environments to human-made surfaces, which can alter the thermal properties of surfaces, urban energy balance, microclimate, moisture available in cities, and air quality (Rizwan, Dennis, and Chunho 2008; Firozjaei et al. 2018a; Ezimand, Kakroodi, and Kiavarz 2018). Recent studies show that the overall CO₂ level has increased by 31% in a couple of centuries ago. Furthermore, the mean temperature has increased 0.8-degree Celsius in the past century (Firozjaei et al. 2018b). One of the major environmental outcomes of urbanization is the urban heat island (UHI) (Firozjaei et al. 2018a). It refers to the phenomenon of high urban atmospheric and surface temperatures compared to the suburban or rural areas (Voogt and Oke 2003; Yuan and Bauer 2007; Firozjaei et al. 2018a). In 1833, Luke Howard defined the concept of urban heat island for the first time (Howard 1833). Since then, numerous studies have been conducted on the UHI (Yuan and Bauer 2007; Imhoff et al. 2010; Schwarz, Lautenbach, and Seppelt 2011; Quan et al. 2014; Huang et al. 2016; Zhou, Rybski, and Kropp 2017). From the middle of the twentieth century, the phenomenon of UHI has grown dramatically in large cities (Akbari, Pomerantz, and Taha 2001; Stone 2008); with the development of urbanization, temperature changes have increased in various urban areas (Georgescu et al. 2011; Quan et al. 2014; Shen et al. 2016; Huang et al. 2016). The UHI has a serious impact on urban flora (Knapp et al. 2010), climate (Parker 2010; Mackey, Lee, and Smith 2012), concentration of pollutants (Santamouris 2015), air quality (Lo and Quattrochi 2003; Grimm et al. 2008), energy and water consumption (Guhathakurta and Gober 2007; Rizwan, Dennis, and Chunho 2008), human health (Tan et al. 2010), heat-related deaths (Changnon, Kunkel, and Reinke 1996; Ho, Knudby, and Huang 2014), human thermal comfort (Laforteza et al. 2009; Tan et al. 2010; Steeneveld et al. 2011), environmental and economic impacts (Rizwan, Dennis, and Chunho 2008), and global warming (Li et al. 2016); thus, it can have a massive effect on the quality of urban life (Shen et al. 2016).

UHIs manifest themselves in different forms in a city and its rural hinterlands, including: (1) canopy layer heat island (CLHI); (2) boundary layer heat island (BLHI); and (3) surface urban heat island (SUHI). While the urban boundary layer is located above the canopy layer, the urban canopy layer is roughly stretching upwards from the surface to mean building height (Voogt and Oke 2003). Since CLHI and BLHI explain the warming of the urban atmosphere, they are referred to as atmospheric heat islands, while the relative warmth of urban surfaces in comparison with surrounding rural areas is the feature of SUHI. In the stated comparison it is clear that atmospheric UHIs are larger at night, while surface UHIs are larger at day (Roth, Oke, and Emery 1989). Atmospheric heat islands are typically measured by in situ sensors of air temperature through weather station networks or mobile transverse, while SUHI is regularly described by land surface temperature (LST) that is acquired through airborne or satellite thermal infrared data, which provisions a synoptic and repeated way of studying the effect of SUHI at various spatial and temporal scales. Although thermal data are recorded frequently by synoptic stations, these data lack a suitable spatial resolution (Firozjaei et al. 2018a). Study of the SUHI using remote sensing data is useful for analyzing spatial and temporal variability of UHI (Liu and Zhang 2011; Firozjaei et al. 2018a). Thus, remote sensing has become a practical tool for SUHI studies in recent decades (Cao et al. 2008; Deng and Wu 2013; Li et al. 2016; Zhou, Rybski, and Kropp 2017; Firozjaei et al. 2018a).

In the SUHI studies, the spatial and temporal variability of SUHI is one of the most important issues. Many indicators have also been developed to quantify the variations, such as the use of difference between urban and rural mean temperatures, magnitude, extent, and thermodynamic landscape index (Tran et al. 2006; Imhoff et al. 2010; Zhou et al. 2011; Schwarz, Lautenbach, and Seppelt 2011). Moreover, several other indicators have been

extended, including: the variety urban–water (Chen et al. 2006), the hot island area (Zhang and Wang 2008), the fitted three-dimensional Gaussian properties (Streutker 2002), and the LST magnitude (Rajasekar and Weng 2009). Some of remote sensing indicators do not use the urban and rural priori concepts. It should be noted that the use of various sensors to study the SUHI variations led to different spatial resolutions for thermal emission. In sum, previous studies have used different indicators, seasons and time of day for assessing the surface UHI (Weng 2009). A comparison analysis of SUHI is more complicated as different spatial extents of studies are considered. A review of previous studies shows that much effort has not been made to develop simple statistical models that can be applied to long-term remote sensing image data to analyze the spatial and temporal variations of SUHI (Schwarz, Lautenbach, and Seppelt 2011; Quan et al. 2014; Firozjaei et al. 2018a).

Pearson's chi-square statistics (Almeida et al. 2005; Bonham-Carter 2014) and Shannon's entropy index have been used to determine the built-up expansion/sprawl (Lata et al. 2001; Li and Yeh 2004; Kumar, Pathan, and Bhanderi 2007) in previous studies. The earlier studies used chi-square and entropy for determining the overall freedom of built-up expansion pattern. Almeida et al. (2005) and Yeh and Li (2001) used different forms of entropy to analyse spatial restructuring of land use patterns. Also, entropy index was used to determine the built-up sprawl pattern (Yeh and Li 2001; Sudhira, Ramachandra, and Jagadish 2004; Almeida et al. 2005; Kumar, Pathan, and Bhanderi 2007). These indices were basically employed to analyse urban form with respect to built-up land. The present study explored how the chi-square and entropy indices could be used as a measure to analyse the SUHI variations. Additionally, degree-of-goodness was also proposed to combine the chi-square and entropy as they were determined in different scales and analysed the variations from different aspects. Degree-of-goodness index represents the degree of regularity and homogeneity of the variations of a parameter in spatial and temporal dimensions. If the value of this index is positive, the degree of regularity and homogeneity of the variations are high and appropriate (Bhatta, Saraswati, and Bandyopadhyay 2010).

Specifically, the objectives of this research were: (1) introducing a new strategy of study through Pearson's chi-square and Shannon's entropy in order to assess the degree-of-freedom and degree-of-sprawl in urban LST classes and SUHI, and (2) developing a new index, degree-of-goodness, that merged the two preceding ones into a single measure to investigate spatial and temporal variation of the SUHI simultaneously.

2. Study area

The city of Babol, Iran, is located in the Northern part of Iran. Geographically, it lies from 52°37'16" to 52°43'02" E longitude and from 36°30'49" to 36°35'1" N latitude, with the area of 6666.66 hectares (Figure 1). The Babol city is placed between the Caspian Sea and Alborz mountains, at a distance of 15 km from the Caspian Sea and 210 km northeast of Tehran. The elevation of the city was 2 meters below the mean sea level. The city was chosen for this study, because of its steadily annual population growth rate of 7% as a result of population growth and immigration from the rural. Urbanization had resulted in excessive and unplanned construction, changes in the physical form of the city and its expansion in different directions. Physical growth had led to numerous changes in urban built-up land and suburban agricultural land use. Eventually, several major problems, such as adversity in usage, urban environmental disorder and the vanishing of suburban agricultural lands into urban land (e.g., residential or industrial) had taken place. The rise of the surface temperature is among the adverse effects of changes in green space and agricultural land into urban built-up land (Firozjaei et al. 2018a; Panah, Kiavarz Mogaddam, and Karimi Firozjaei 2017).

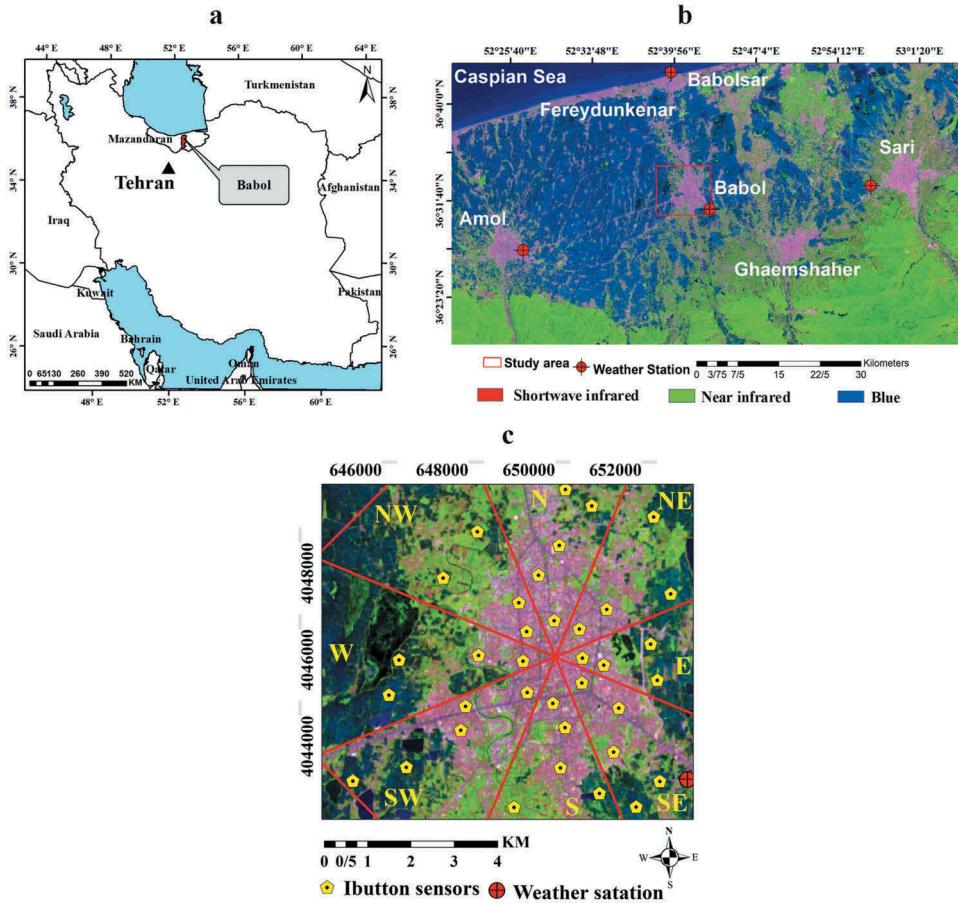


Figure 1. The study area: (a) Location of the Babol city in Iran; (b) location of the study area relative to the surrounding cities in the false color composite image (Shortwave Infrared, Near infrared and Red bands) of the Landsat 8 OLI for 2017; (c) The false color composite image (Shortwave Infrared, Near infrared and Red bands) of the Landsat 8 OLI for 2017 of the studied area and the location of the air temperature recording devices.

3. Data and methods

The methodologies applied to achieve the current study objectives are presented in Figure 2.

3.1. Data

Five Landsat images from 1985, 1992, 2001, 2008 and 2017 were acquired for this study. They were chosen because the time intervals between the imaging years for climate background were similar. The daily average of air temperature, relative humidity, wind speed and solar radiation data for the days which related to the images date were investigated (“www.mazmet.ir”). The results showed that climatic parameters did not have high variation. In addition, the weather conditions showed that for at least 4 days

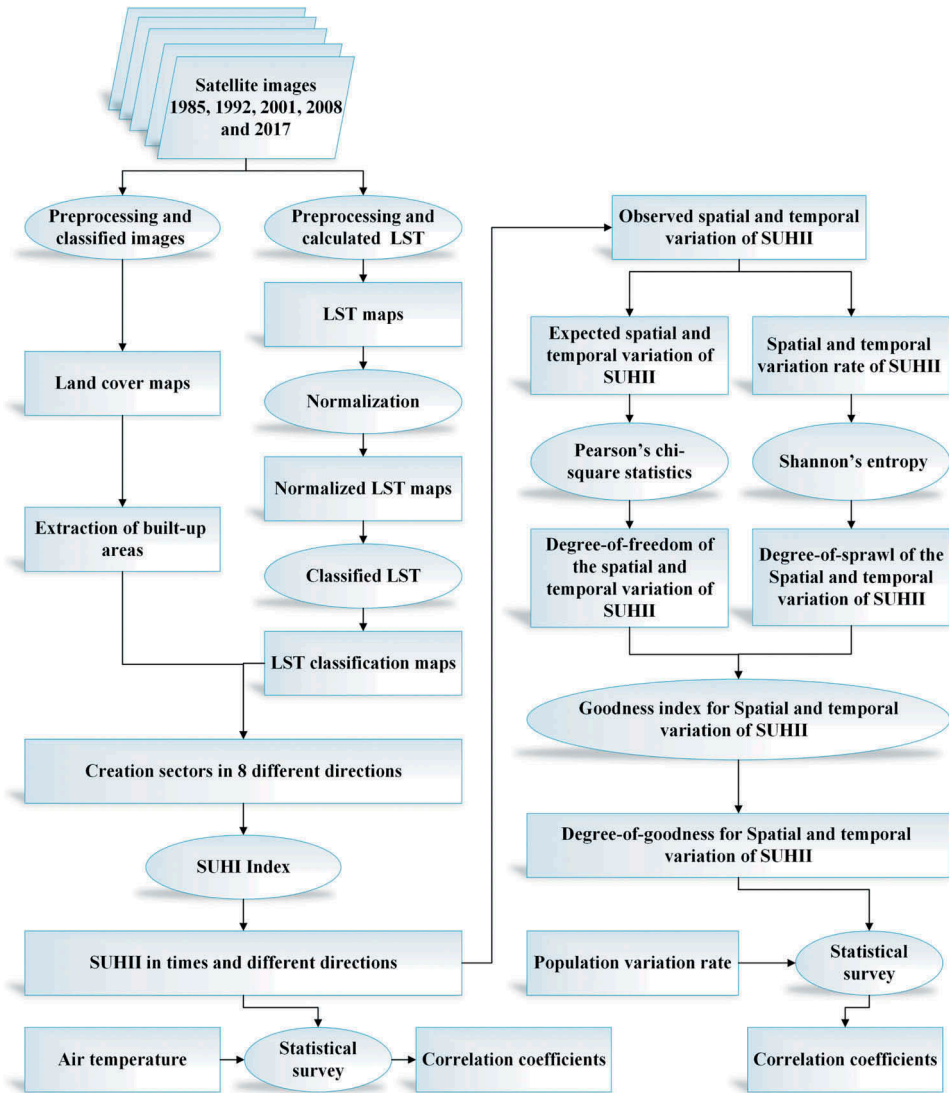


Figure 2. The analytical procedures of the study.

before the selected imaging dates, there was no rainfall in the study city. Due to the proximity of the study area to the sea, forests and mountains, the number of cloudy days was high. All Landsat images of the region for the period 1985 to 2017 had been checked. Spring was the most suitable season for selecting images to have the least variation in climate parameters such as air temperature, relative humidity, cloudiness and wind speed. The images were georeferenced in UTM coordinate system and located in zone 39N. The downloaded data from the USGS included the highest quality Level-1 Precision Terrain (L1TP) data which were considered suitable for time-series analysis. The geo-registration was consistent and the root mean square error (RMSE) less than 12 meters (≤ 0.5 pixel) (Moghaddam et al. 2018; Weng et al. 2019).

Air and soil temperature data were acquired for free by the meteorological organization of Mazandaran (“www.mazmet.ir”) for the weather station (see [Figure 1](#)). The geographic location of the synoptic station was located in one pixel of the thermal band of Landsat imagery (rescaled to 30×30 m) with homogeneous land cover (grass). The location was completely flat, outside the urban area.

The Moderate Resolution Imaging Spectroradiometer (MODIS) Atmospheric Profiles products (MOD 07), containing the following features: (1) total-ozone burden; (2) atmospheric stability; (3) temperature and moisture profiles; (4) and atmospheric water vapour, were exploited to complete the input parameters, and estimation of LST maps from satellite images. Because the MOD07 product did not exist for the years before 2000, radiosonde data was used to calculate the LST to 1985 and 1992. Radiosonde had been launched at the synoptic Station at a time close to the satellite overpass time for 14/05/1985 and 18/06/1992, at 9:50 and 9:55 local time, respectively.

To complete the input parameters for the purpose of the evaluation of the LST maps, LST product of MODIS (MOD 11) was also considered. The MOD 11 daily data are retrieved at 1-km pixels by the generalized split-window algorithm. In the algorithm, emissivity values in bands 31 and 32 were estimated from land cover classes, atmospheric column water vapor and lower boundary air surface temperature were separated into tractable sub-ranges for optimal retrieval. The product was comprised of LST, quality assessment, observation time, view angles, and emissivity.

For the accuracy assessment and comparison of the UHI in different geographic directions in 2017, a set of air temperature data recorded by 36 ground devices (Eletich RC-5) at the time of satellite passes over study area were used. The geographic location of each air temperature recording device in the study area is shown in [Figure 1c](#). The locations of the devices were selected to have an even distribution along different geographic directions. Four to five devices were located in any geographical direction. More devices were located in the geographic directions with more built-ups. However, for each geographic direction, there were at least two devices located in the built-up areas and two devices in the suburban areas.

The devices were placed at a height of 2 meters from the ground to record air temperature. These devices recorded temperature with precision of 0.5°C in the range from 20°C to 40°C , and precision 1°C for temperatures outside the range (Weng et al. 2019). The locations of the air temperature recorders in the study area were determined by using a mobile GPS device with a planimetric error less than 6 meters. The utilized data are presented in [Table 1](#).

3.2. Methods

3.2.1. Pre-processing and built-up land extraction

Atmosphere correction of satellite imagery was performed using FLAASH algorithm (Cooley et al. 2002). This module employs the MODTRAN 6 model (Berk et al. 2014). The classes of land cover in the study area were identified based on field observations supported by the knowledge of the researchers about the area. These classes included built-up land, agricultural land, green space, and bodies of water. By visual interpretation of false color composite image (shortwave infrared, near infrared and red bands) of the Landsat imagery, topographic maps and orthophoto for each year (1985, 1992, 2001, 2008 and 2017), training and validation data were carefully selected for these classes. For each land cover class, more than 100 pixels were selected as a set of training and validation samples for classification and evaluation of accuracy. Maximum likelihood (ML)

Table 1. Data sets for this study.

Data type	Satellite (sensor)	Resolution, Scale	Date	Local Time overpass
Satellite images	Landsat 5 TM	30 m	14/05/1985	10:08:12 (Day)
Satellite images	Landsat 5 TM	30 m	18/06/1992	10:01:24 (Day)
Satellite images	Landsat 7 ETM+	30 m	03/06/2001	10:17:48 (Day)
Satellite images	Landsat 5 TM	30 m	30/06/2008	10:15:34 (Day)
Satellite images	Landsat 8 OLI/TIRS	30 m	06/05/2017	10:07:20 (Day)
Topographic map	-	1:2000	1985–2017	-
Orthophoto	-	1:1000	1985–2017	-
Population map	-	-	1985–2017	-
Air temperature	Weather station (during the satellite overpass)	-	1985–2017	-
Soil temperature	Weather station (during the satellite overpass)	-	1985–2017	-
Climatic parameters	Weather station (during the satellite overpass)	-	1985–2017	-
Water vapor (MOD 07)	Terra (MODIS)	5000 m	2001–2017	-
LST (MOD 11)	Terra (MODIS)	1000 m	2001–2017	-
Water vapor	Weather station Ground-based atmospheric data	-	1985–1992	-

classifier was used to classify the images (Firozjahi et al. 2018a). After the image classification process, accuracy assessment was performed through comparing with validation data selected for these classes from topographic map and orthophoto for each year, separately. The Overall Accuracy (OA), kappa coefficient for land use maps and the user and producer accuracy for the built-up land-cover class (Otukey and Blaschke 2010; Moghaddam et al. 2015) were computed for each year. Finally, the area of each type of land cover was extracted from classified images. The built-up land was extracted from all classification maps. In order to recognize changes during the studied period, classified images were compared in a GIS environment.

3.2.2. LST retrieval

A systematic methodology was required to estimate LST from the Landsat 5 TM, Landsat 7 ETM+ and Landsat 8 TIRS data. Because the thermal band 11 of Landsat 8 has a data bias in the estimation of LST (Barsi et al. 2014), in this study, LST was estimated using the SC method for band 10 of Landsat 8 TIRS. The DN (digital number) value of pixels was converted into at-sensor spectral radiance (L_s) as a preparatory step for thermal image processing. By the use of the inverted Planck's Law with an assumption that the Earth's surface is a black body with an emissivity value equal to 1 (Li et al. 2011; Walawender et al. 2014), the at-sensor spectral radiance was converted to at-sensor brightness temperature (T_s). For final LST retrieval, a single-channel (SC) LST estimation algorithm (Sobrino, Jiménez-Muñoz, and Paolini 2004; Walawender et al. 2014) (Equation (1)) was applied.

$$\text{LST} = \gamma \left[\frac{1}{\varepsilon} (\psi_1 L_s + \psi_2) + \psi_3 \right] + \delta \quad (1)$$

In this algorithm, ε is land surface emissivity (LSE), L_s is at-sensor spectral radiance, T_s at-sensor brightness temperature and γ and δ are the Planck's function-dependent parameters can be estimated through Equations (2) and (3) (Jiménez-Muñoz and Sobrino 2003; Jiménez-Muñoz et al. 2014; Firozjahi et al. 2018a):

$$\gamma = \left\{ \frac{c_2 L_s}{T_s^2} \left[\frac{\lambda^4 L_s}{c_1} + \frac{1}{\lambda} \right] \right\}^{-1} \tag{2}$$

$$\delta = -\gamma \times L_s + T_s \tag{3}$$

Where c_1 ($1.19104 \times 10^8 \text{ W } \mu\text{m}^{-4} \text{ m}^{-2} \text{ sr}^{-1}$) and c_2 ($1.438773 \times 10^4 \text{ } \mu\text{m k}$) are the Planck’s radiation constants and λ stands for the effective wavelength of the thermal bands ($\lambda = 11.457$ for Landsat 5 TM, $\lambda = 11.270$ for Landsat 7 ETM+ and $\lambda = 10.904$ for Landsat 8/TIRS B1).

Here, the applied SC algorithm was unique as it incorporated atmospheric correction and considered different emission properties of the surfaces. ψ_1 , ψ_2 , and ψ_3 are the atmospheric functions related to the water vapor content of the atmosphere. They can be calculated by the use of Equations (4) and (5) (Jiménez-Muñoz and Sobrino 2003; Jiménez-Muñoz et al. 2014; Firozjaei et al. 2018a):

$$\begin{cases} \psi_1 = 0.14714w^2 - 0.15583w + 1.1234 \\ \psi_2 = -1.1836w^2 - 0.37607w - 0.52894 \text{ for TM and ETM} \\ \psi_3 = -0.04554w^2 + 1.8719w - 0.39071 \end{cases} \tag{4}$$

$$\begin{cases} \psi_1 = 0.04019w^2 + 0.02916w + 1.01523 \\ \psi_2 = -0.38333w^2 - 1.50294w + 0.20324 \text{ for TIRS} \\ \psi_2 = 0.00918w^2 + 1.36072w - 0.27514 \end{cases} \tag{5}$$

The obtained water vapor data in this study were from the MOD07 water vapor data product for 2001 to 2017 and from ground-based atmospheric radio sound data for 1985 and 1992.

A popular method for calculating LSE is the Normalized Difference Vegetation Index (NDVI)–based method. This method was presented in (Sobrino and Raissouni 2000; Sobrino et al. 2008; Jiménez-Muñoz et al. 2014). In this method, LSE is obtained by thresholding on NDVI and Fractional Vegetation Cover (FVC). To calculate NDVI, Equation (6) was used (Tucker 1979).

$$NDVI = \frac{\rho_{NIR} - \rho_{Red}}{\rho_{NIR} + \rho_{Red}} \tag{6}$$

Where ρ_{NIR} and ρ_{Red} are the ground reflectance of near- infrared and red bands. The values of this index vary between -1 and $+1$.

To calculate FVC, Equation (7) was used (Jiménez-Muñoz et al. 2014).

$$FVC = \left(\frac{NDVI - NDVI_S}{NDVI_V - NDVI_S} \right)^2 \tag{7}$$

Where $NDVI_V$ is related to dense vegetation and $NDVI_S$ is related to dry soil. After obtaining fractional vegetation cover, thermal bands of Landsat TM, ETM+ and TIRS and

Equation (8) were used to calculate LSE (Jiménez-Muñoz et al. 2014; Sobrino et al. 2008; Walawender et al. 2014; Firozjaei et al. 2018a).

$$\begin{aligned}
 \text{FVC} = 0 \quad \text{LSE} &= a_\lambda + b_\lambda \rho_{\text{Red}} \\
 0 < \text{FVC} < 1 \quad \text{LSE} &= \varepsilon_{v\lambda} \text{FVC} + \varepsilon_{s\lambda} (1 - \text{FVC}) + C_i \\
 \text{FVC} = 1 \quad \text{LSE} &= \varepsilon_{v\lambda} + C_i \\
 \text{NDVI} < 0 \quad \text{LSE} &= \text{Emissivity Water}
 \end{aligned} \tag{8}$$

where ρ_{Red} is reflectivity in the red band, a_λ and b_λ are channel dependent regression coefficients, FVC is fractional vegetation cover, a and b are linear correlation coefficients between red band reflection with LSE, $\varepsilon_{s\lambda}$ and $\varepsilon_{v\lambda}$ are the soil and vegetation emissivity at wavelength λ (extracted from the Advanced Spaceborne Thermal Emission and Reflection Radiometer (ASTER) spectrum library) and C_i is a term which takes the cavity effect into account due to the surface roughness ($C_i = 0$ for flat surfaces) (Sobrino et al. 2008).

Finally, soil temperature was recorded at the meteorological station and the MOD11 product was used to evaluate the accuracy of the calculated LST. According to (Qin et al. 2011; Srivastava, Majumdar, and Bhattacharya 2009), if the difference between the average LST calculated from Landsat and that obtained from the MODIS Product is less than 2 °C, it indicates that the LST calculated with Landsat image is acceptable.

3.2.3. Normalized LST computation and classification

To further study the SUHI changes of the city in the time periods, a change detection technique had to be applied to the five thermal infrared images. However, it was difficult to compare these images directly using the LST computed in Section 3.2.2 due to the climate background (soil humidity due to the month rainy, air temperature, wind circulation, solar irradiation) partial difference between five images. To solve this problem, a normalization technique and a surface urban heat island ratio index were used. The SUHI study is usually focused on the spatial distribution patterns of relative temperature difference. The climate background difference can only affect the absolute temperature values but not affect the distribution pattern of the temperature. Therefore, normalization to the five images with different climate backgrounds could rescale the radiant temperature to the same level between 0 and 1 and thus reduce the climate background difference. By utilizing maximum and minimum temperature parameters, all images were normalized using Equation (9) (Weng, Rajasekar, and Xuefei 2011):

$$\text{NLST}_i = \frac{\text{LST}_i - \text{LST}_{\min}}{\text{LST}_{\max} - \text{LST}_{\min}} \tag{9}$$

Where NLST_i is the normalized land surface temperature of i pixel, LST_i the land surface temperature of i pixel, LST_{\min} the minimum and LST_{\max} the maximum LST value in an image.

By the use of the mean value and the standard deviation, normalized land surface temperatures were classified into five temperature classes (Firozjaei et al. 2018a). In Table 4, T_{mean} is the mean of NLST, and STD is the standard deviation value.

After classifying the NLST data for each image, the area value of each temperature class was calculated, and changes in each temperature class area during the studied period

were investigated. The major purpose of normalizing and then classifying surface temperature data was to understand changes in the statistical distribution of temperature data and through that diminish the SUHI changes.

3.2.4. SUHI intensity computation

For many cities, built-up growth rates in geographical directions is different (Dadras et al. 2015; Bhatta, Saraswati, and Bandyopadhyay 2010). Consequently, the trend of the SUHI variations for the geographical directions in a time period is not the same. Therefore, the computation of indices for analysing the SUHI variations in different cardinal directions provided valuable information in urban planning.

The downtown was considered as the reference to define the main built-up region of the city. After that, a large buffer was drawn around this point, so that the radius of the buffer to include all pixels related to the built-up land at the time of last satellite imaging, i.e., on 06/05/2017. This circular area was divided into geographic directions of north (N), south (S), southeast (SE), southwest (SW), west (w), east (E), northeast (NE), northwest (NW) (Dadras et al. 2015). The SUHII was then computed for various cardinal directions and in different times. In order to analyse the changes in SUHII from 1985 to 2017, the surface urban heat island ratio index was further used (Han-Qiu and Ben-Qing 2004). The SUHII was calculated using Equation (10) (Xu and Chen 2003; Cao et al. 2008; Firozjaei et al. 2018a).

$$\text{SUHII} = \frac{1}{100m} \sum_{i=1}^n W_i P_i \quad (10)$$

Weights are considered according to the class number and in the formula m is the classes' number of the normalized temperature (according to Table 4: $m = 5$) and n is the number of temperature classes that are higher than the average temperature (according to Table 4: $n = 2$). W_i is the weight of temperature classes higher than the normal condition. The weight value showed the LST classes which were higher than normal (the medium temperature class). The weight of each class was equal to the row number of the class, for example the weight value of class 4 (high temperature class) was 4 and the weight value of class 5 (very high temperature class) was 5. P_i indicates the ratio of the areas with temperature classes higher than a normal condition to the total area of the built-up areas (Firozjaei et al. 2018a). Actually, to calculate this index, the area of the built-up lands located in the very high temperature class is much more effective than the area of the built-up lands on the high temperature class and has a higher weight. The value of this index varies from 0 to 1 (Xu and Chen 2003; Cao et al. 2008; Firozjaei et al. 2018a). If the total area of the built-up lands located in high and very high temperature classes, the value of this index is 1, and if no area of built-up lands located in high and very high temperature classes, then the index value will be 0.

For the accuracy assessment and comparison of the UHI in different geographic directions in 06/05/2017, a set of air temperature data recorded by 36 ground devices at the time of satellite passes was used. This assessment was carried out for a single date. In the first step, the mean temperature for the urban and suburbs built-up land was calculated for each geographic direction separately. In the next step, for each geographic direction, the difference in the mean air temperature between the urban and suburbs built-up was calculated. In the final step, the relationship between the mean air temperature of the urban and that of the suburbs and the values of SUHII were analyzed for different geographic directions.

3.2.5. Evaluation of indices for analysing SUHI variations

The observed SUHII variation ratio value was calculated according to equation (11). To calculate the observed variation ratio for a particular geographic direction, the SUHII value for that direction in the second year (e.g. 2008) should be divided by the SUHII value in the first year (e.g. 2001) for same direction and multiplied by 100. As a result, the unit value was percent.

$$\text{Observed SUHII variation ratio} = \frac{\text{SUHII2 (secondyear)}}{\text{SUHII1 (firstyear)}} \times 100 \quad (11)$$

If SUHI increases for a particular direction in the second year versus the first year, the variation ratio value is greater than 100, and if the SUHI for a particular direction in the second year is less than the first year, the variation ratio value will be less than 100.

- Difference between the observed and expected SUHII variation

Observed variation ought to be compared with expected variation to understand the discrepancy. Table A1 shows the observed SUHII variation in Babol city. From table A1, the theoretical expected urban growth can be estimated by employing Equation (12).

Let the Table A1 be called matrix R, each of the matrix elements illustrates R_{ij}^E , $i = 1, 2, 3, \dots, n$ (Matrix rows or particular directions) and $j = 1, 2, 3, \dots, m$ (the matrix columns or the particular time periods), R_i^s is the sum of rows i , $R_j^s R_j^s$ is column total, and $R_g = \sum_{i=1}^n \sum_{j=1}^m R_{ij}$ (Dadras et al. 2015; Bhatta, Saraswati, and Bandyopadhyay 2010). The expected SUHII variation for each variable was calculated by the products of marginal totals, divided by the grand total.

$$R_{ij}^E = R_i^s \times R_j^s / R_g \quad (12)$$

- Shannon's entropy index

The physical concept of entropy in a system represents the degree of order in that system. In this study, the SUHII variation in cardinal directions and different time periods was considered as a system. The entropy was used to determine the order of the SUHII variation in different cardinal directions and time periods. If the entropy value of the SUHII variation were high for a particular geographic direction, it would indicate the irregular trend in SUHII variation for that particular geographic direction in the particular time period. If the entropy of the SUHII variation were high for a specific time period, it would represent an irregular trend in SUHII variation over that time period in different cardinal directions. This index calculated the degree of stability in SUHII variation trend for different cardinal directions and time intervals.

Shannon entropy has been used as a method to determine built-up growth pattern in previous studies (Kumar, Pathan, and Bhanderi 2007; Li and Yeh 2004) and is used to delineate the sprawl built-up growth value. In this study, Shannon's entropy was calculated for each cardinal direction according to the SUHII variation using Equation (13):

$$H_j = - \sum_{i=1}^n P_i \log_e(P_i) \quad (13)$$

Where P_i is the proportion of the variable in the i th column (i.e., the SUHI variation ratio in i th direction), and n the number of cardinal directions equal to 8.

The degree-of-sprawl of SUHI variation was computed by the value of Shannon's entropy. The value of Shannon's entropy varied from 0 to $\ln(n)$. Whenever the Shannon's entropy value is closer to zero, it demonstrates the compressed distribution of the SUHI variation values; a value close to $\ln(n)$ indicates the sprawl distribution of the SUHI variation values. High entropy values indicate the occurrence of extreme sprawl SUHI variation. The Shannon's entropy value of each time period was computed using the following Equation (14) (Bhatta, Saraswati, and Bandyopadhyay 2010; Dadras et al. 2015).

$$H_i = - \sum_{j=1}^m P_j \log_e(P_j) \quad (14)$$

Where P_j is the proportion of the variable in the j th column (i.e., the SUHI variation ratio in j th period), and m the number of time periods (equal to 4).

The overall degree-of-sprawl of the SUHI variation values could be computed as (Bhatta, Saraswati, and Bandyopadhyay 2010):

$$H = - \sum_{i=1}^n \sum_{j=1}^m P_{ij} \log_e(P_{ij}) \quad (15)$$

Where P_{ij} is the proportion of the variable in the i th row and the j th column (ratio of the SUHI variation in the j th time period and i th cardinal direction).

- Degree-of-freedom index

The degree-of-freedom of SUHI variation reflected the difference between the observed and expected SUHI variation. The high degree of deviation indicated that the variable was independent of other variables in the class (Bhatta 2009). Pearson's chi-square statistics takes into account the checking of freedom amongst pairs of variables chosen to explain the same category of land-cover change (Almeida et al. 2005). The degree-of-freedom was determined by performing chi-square test. It revealed the freedom or degree of deviation for the observed SUHI variation over the expected. To compute the chi-square statistics in different time periods, the following Equation (16) was used (Bhatta 2009).

$$X_j^2 = \sum_{i=1}^n (R_i - R_i^E)^2 / R_i^E \quad (16)$$

Where X_j^2 is the degree-of-freedom for the j th time period, R_i is the observed SUHI variation in the i th row for a specified column, R_i^E is the expected SUHI variation in the i th row for a specified column.

When replacing i (row) with j (column) and n (number of rows) with m (number of columns) in Equation (16), we can set the degree-of-freedom for each cardinal direction

(X_j^2) separately. The overall degree-of-freedom of SUHII variation can be computed using Equation (17) (Bhatta, Saraswati, and Bandyopadhyay 2010):

$$X^2 = \sum_{i=1}^n \sum_{j=1}^m (R_{ij} - R_{ij}^E)^2 / R_{ij}^E \quad (17)$$

The degree-of-freedom value indicated heterogeneity in SUHII variations. The chi-square has a lower limit of 0, when the observed value exactly equals the expected value. Higher overall freedom indicates lack of equal weightage and lack of consistency in planning with the entire city in consideration. Higher degree-of-freedom for a cardinal direction is an indication of unstable development within the cardinal direction with the change of time. Higher degree-of-freedom for a time period can be considered as higher variability in inter-cardinal direction in SUHII.

- Degree-of-goodness index

Since chi-square (degree-of-freedom) and entropy (degree-of-sprawl) were different and in some specific cases may contradict with one another, additional index was employed, referring to as the degree-of-goodness of SUHII variation. The degree-of-freedom index and the Shannon's entropy were combined to produce this index (Dadras et al. 2015; Bhatta, Saraswati, and Bandyopadhyay 2010). This index can be computed using Equation (18):

$$G_j = \log_e \left[\frac{1}{X_j^2 (H_j / \log_e(n))} \right] \quad (18)$$

Where G_j is the degree-of-goodness of SUHII variation for the j^{th} time period, X_j^2 the degree-of-freedom for the j^{th} time period, H_j the entropy for the j^{th} time period, and nn the total number of cardinal directions. Replacing j with i and n with m in Equation (18) was considered appropriate to calculate the degree-of-goodness of SUHII variation for each cardinal direction. The overall degree-of-goodness will also be calculated using Equation (19) (Bhatta, Saraswati, and Bandyopadhyay 2010):

$$G = \log_e \left[\frac{1}{X^2 (H / \log_e(m \times n))} \right] \quad (19)$$

Where X^2 is the overall degree-of-freedom and H the overall degree-of-sprawl. The degree-of-goodness is the result of a combination of degree-of-freedom and degree-of-sprawl. For this reason, by computing this index can generally analyse the arrangement at SUHII variation and the difference in observed and expected SUHII variations in spatial and temporal dimensions.

Finally, to analyse the SUHII variation in spatial and temporal dimensions of Babol city from 1985 to 2017, degree-of-sprawl, and degree-of-freedom and degree-of-goodness indices of SUHII variation were all computed. To investigate the effect of population increase on SUHII variation in spatial and temporal dimensions, the correlation coefficient between the population variation and the degree-of-goodness index values was calculated for different time periods and cardinal directions.

4. Results

4.1. Land cover classification result

The result of land cover classification for the utilized images are presented in Figure 3. Generally, the city’s expansion led to the destruction of other land uses, especially agricultural land.

The error matrix, overall accuracy, and kappa coefficient for each classified image and the user and producer accuracy for the built-up land-cover class for each year were calculated. The area of each class (built-up land, agricultural land, green space and water) and the results of accuracy assessment in different dates are shown in Table 2.

According to Figure 3 and Table 2, agricultural land area had significantly been changed over different dates and a decreasing trend could clearly be observed. A total area of 740.52, 1132.92, and 5.49 hectares of agricultural land was changed into built-up, green space, and water body areas, respectively. These changes of

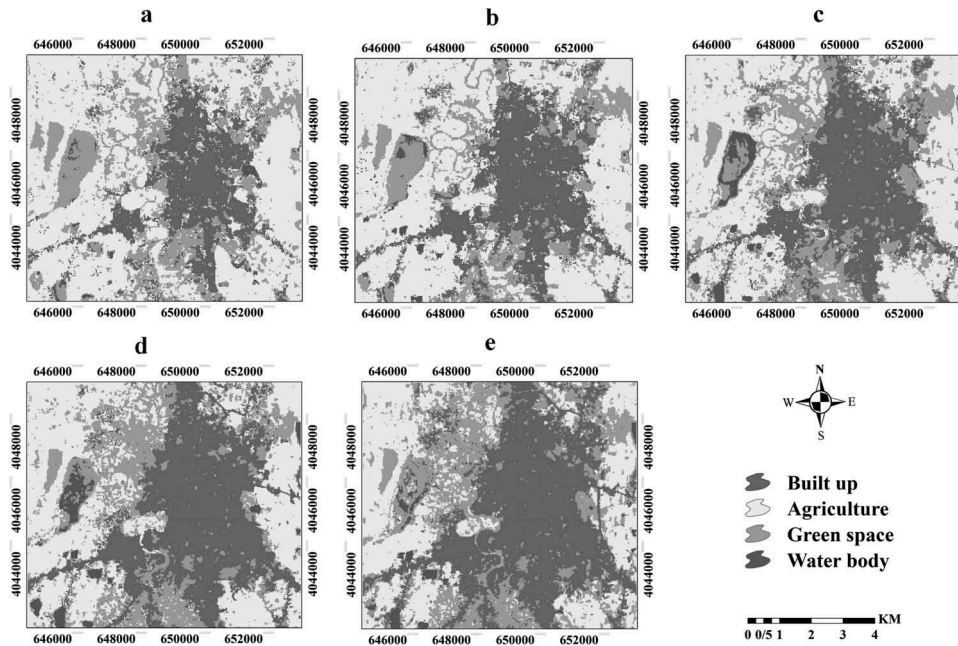


Figure 3. Land cover classification map in (a) 14/05/1985; (b) 18/06/1992; (c) 03/06/2001; (d) 30/06/2008; (e) 06/05/2017.

Table 2. Accuracy of produced land cover maps (Percentage) and land area covered by each class by date (Hectare).

(dd/mm/yyyy)	Built-up	Agriculture	Green Space	Water	User_built-up (%)	Producer_built-up (%)	Kappa coefficient	Overall accuracy (%)
14/05/1985	1265.9	3773.6	1556.5	70.5	91.5	90.8	0.91	92.2
18/06/1992	1622.4	3537.6	1418.9	87.6	90.0	90.0	0.89	90.1
03/06/2001	1808.0	2997.9	1713.8	146.7	92.1	92.3	0.92	93.0
30/06/2008	2226.3	2582.5	1678.5	179.1	93.3	93.7	0.94	94.6
06/05/2017	2535.0	2023.7	1686.5	121.3	91.2	90.8	0.91	91.8

agricultural land were more obvious in the suburbs. In contrast, the green space increased by 25 %, from 1556.55 to 1956.52 hectares. Citrus gardens resulted from the changes in agriculture land were the main reason for green space increase in the suburbs. However, the growth rate of green space land was lower than that of built-up. Built-up land showed a substantial increasing trend from 18% in 14/05/1985 to 38% of the total area in 06/05/2017, which indicates an increase of 1269.14 hectares.

4.2. Land surface temperature

The single-channel (SC) LST estimation algorithm was implemented on satellite images in order to estimate surface temperature maps for the region in time periods are shown [Figure 4](#). Biophysical characteristics of the studied area were very specific. The land use surrounding of the city was agriculture and green space. The important characteristics of these lands were the high amount of greenness and humidity. For this reason, the difference between the surface temperatures of built-up lands and the green space and agriculture surrounding the city during the daytime was very high.

To assess the accuracy of LST maps extracted from satellite images, soil temperature from the weather station at the same time of the satellite overpass were considered. The obtained soil temperature from the weather station and the LST acquired from the single-channel algorithm are shown in [Table 3](#). For more accurate assessment of the LST Extracted from Landsat, the LST product (MOD11) of MODIS was used ([Table 3](#)).

MODIS was launched into Earth orbit by NASA in 1999 on board the Terra (EOSAM) Satellite (Toller et al. 2003). For this reason, for the years 1985 and 1992, the difference between the averages of LST obtained Landsat and MOD 11 is blank in

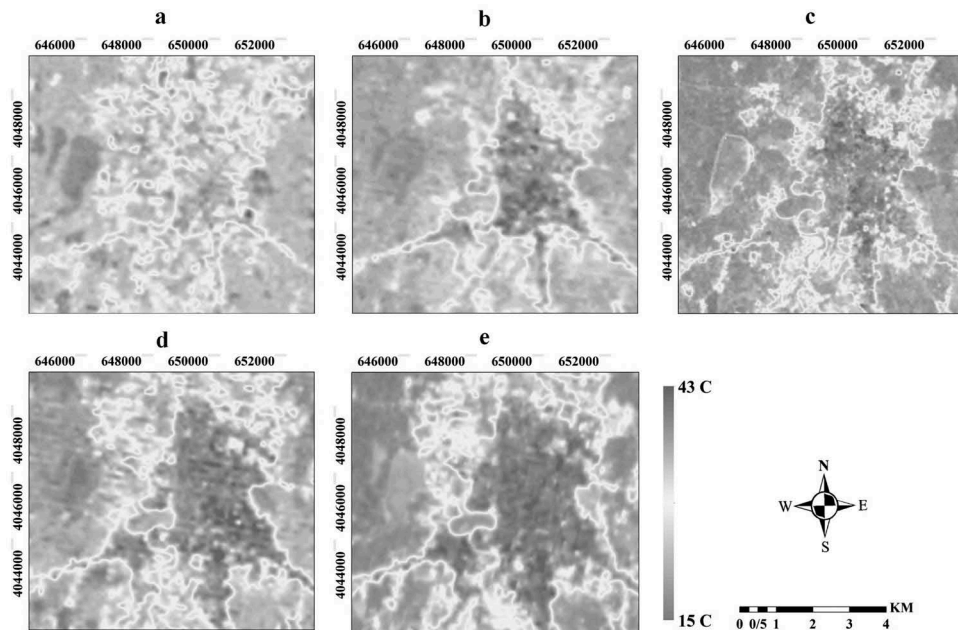


Figure 4. LST map for each time period: (a) 14/05/1985; (b) 18/06/1992; (c) 03/06/2001; (d) 30/06/2008; (e) 06/05/2017 (unit: Centigrade).

Table 3. Comparison of observational LST and LST from satellite images (°C).

Day	14/05/1985	18/06/1992	03/06/2001	30/06/2008	06/05/2017
Observational LST (weather station)	21.3	22.3	22.9	29.1	31.5
Satellite derived LST (Landsat)	22.9	23.8	24.5	27.3	29.1
Average difference (Landsat-MOD11)	-	-	1.81	1.49	1.62
RMSE (Landsat- weather station)			1.80		

Table 3. The difference between the averages LST obtained Landsat and MOD 11 and RMSE between LST obtained Landsat and weather station was less than 1.82 °C. The results of accuracy assessment confirmed the accuracy of the LST maps extracted from satellite images (Qin et al. 2011; Srivastava, Majumdar, and Bhattacharya 2009).

4.3. Normalized land surface temperature classes

The NLST maps are presented in Figure 5. In each map, NLST was classified into five classes using the mean value and the standard deviation.

High- and very high-temperature classes were located around the center of the city and main roads that linked the city and the surrounding towns. The majority of suburbs were covered by the medium-temperature class. The area of each class was calculated in the studied period. Normalized LST values could provide temperature class and its changes were an objective

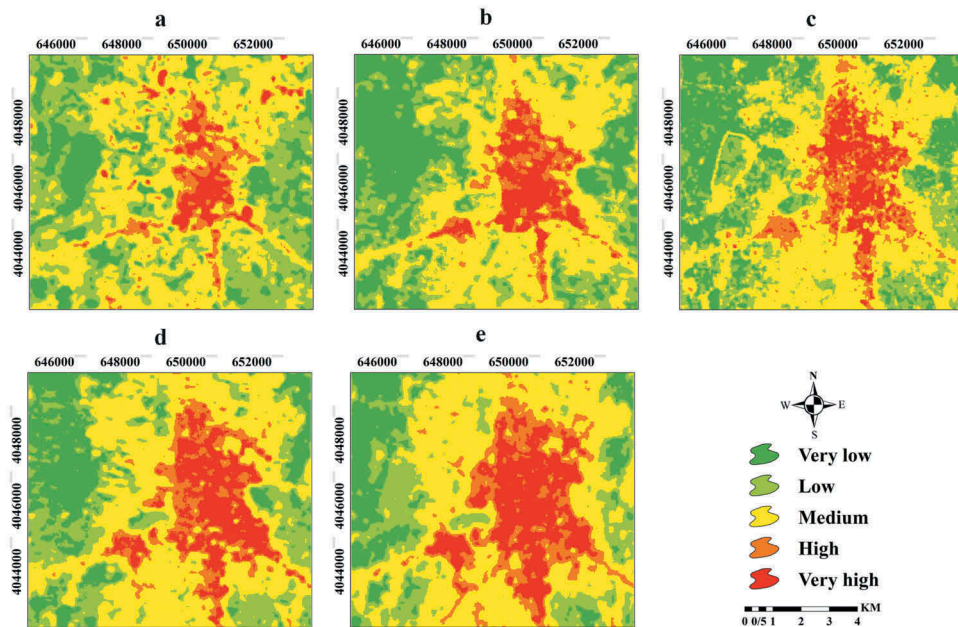


Figure 5. The NLST classification map for (a) 14/05/1985; (b) 18/06/1992; (c) 03/06/2001; (d) 30/06/2008; (e) 06/05/2017.

Table 4. The area of the normalized LST classes (Hectare).

Temperature class Class range	Very low temperature ($T \leq T_{\text{mean}} - 1.5\text{STD}$)	Low temperature ($T_{\text{mean}} - 1.5\text{STD} < T < T_{\text{mean}} - \text{STD}$)	Medium temperature ($T_{\text{mean}} - \text{STD} < T < T_{\text{mean}} + \text{STD}$)	High temperature ($T_{\text{mean}} + \text{STD} < T < T_{\text{mean}} + 1.5\text{STD}$)	Very high temperature ($T > T_{\text{mean}} + 1.5\text{STD}$)
14/05/1985	1142.91	1947.69	2842.92	438.66	294.48
18/06/1992	1709.1	1426.95	2605.05	488.75	436.72
03/06/2001	1449.00	1332.27	2763.81	959.25	461.88
30/06/2008	1213.56	1333.71	2717.28	650.52	751.5
06/05/2017	968.23	1160.60	2840.80	825.38	871.56

comparison of the spatial distribution of the LST values extracting from images that were captured under varied atmospheric, seasonal and illumination conditions (Firozjahi et al. 2018a).

According to Table 4, in all five dates, the medium-temperature class always possessed the maximum area. Along with a decrease in agricultural land, the area of low and very low temperature classes decreased. In contrast, the high and very high-temperature classes were increasing considerably as a result of built-up land cover expansion. Furthermore, population growth, the development of industries, and numerous vehicles in the city and crowded communication roads also contributed to the increase of the high- and very high-temperature classes (Firozjahi et al. 2018a).

4.4. SUHI intensity changes analysis

To analyse SUHI intensity changes in the Babol city during the study period, the SUHI index was used. The SUHI index values for 1985, 1992, 2001, 2008 and 2017 were 0.509, 0.516, 0.547, 0.571 and 0.635, respectively.

The increase of the heat island intensity showed a direct relationship to the population growth with correlation coefficient is 0.90 and, thus, to the rise in the built-up land area.

4.4.1. Analysis of SUHI variation

Figure 6 shows the SUHI in different cardinal directions by date. The main reason for the implementation of indices in different cardinal directions is increasing the efficiency of the results for use in urban planning. According to Figure 6, the geographic direction of the N had a high SUHI in all images whereas the W direction exhibited a low SUHI in the observed periods.

For the accuracy assessment and comparison of the UHI in different geographic directions in 06/05/2017, a set of air temperature data recorded by 36 ground devices at the time of satellite passes was used. The correlation between the two parameters is shown in Figure 7. The correlation coefficient for the cardinal directions yielded 0.82.

Due to the direct relationship between surface temperature and air temperature (Benali et al. 2012; Prihodko and Goward 1997; Vancutsem et al. 2010; García-Cueto et al. 2007), it can be concluded that the air temperature above built-up land is higher than air temperature above agricultural lands and green spaces surrounding the city. This result is consistent with Figure 7. As for the cardinal directions where SUHI is high, the amount of UHI is also high at daytime. These two parameters at daytime have a direct and high correlation with each other.

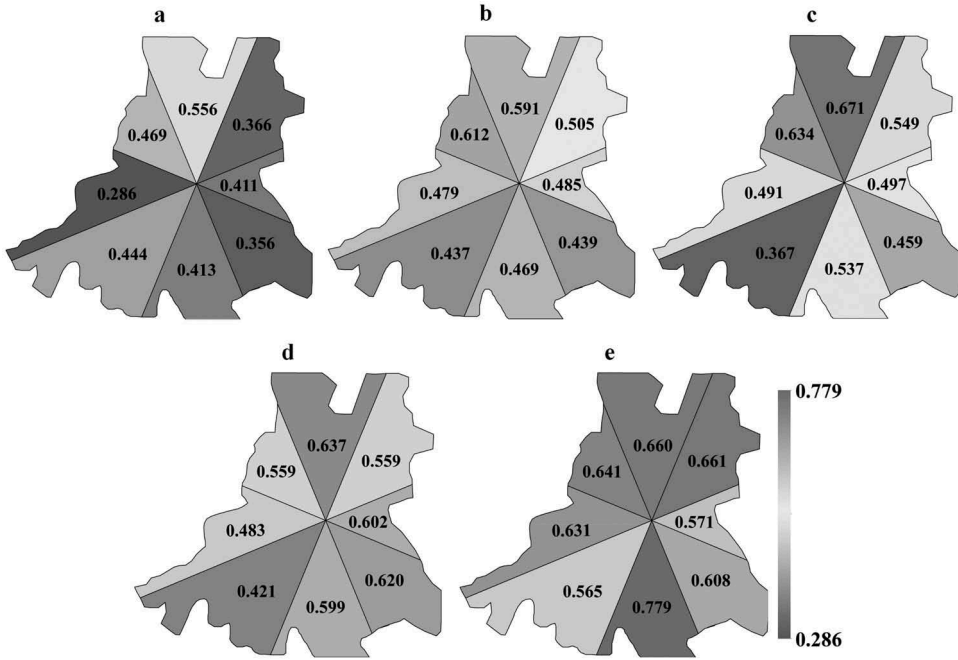


Figure 6. SUHII values in different cardinal directions by day: (a) 14/05/1985; (b) 18/06/1992; (c) 03/06/2001; (d) 30/06/2008; (e) 06/05/2017.

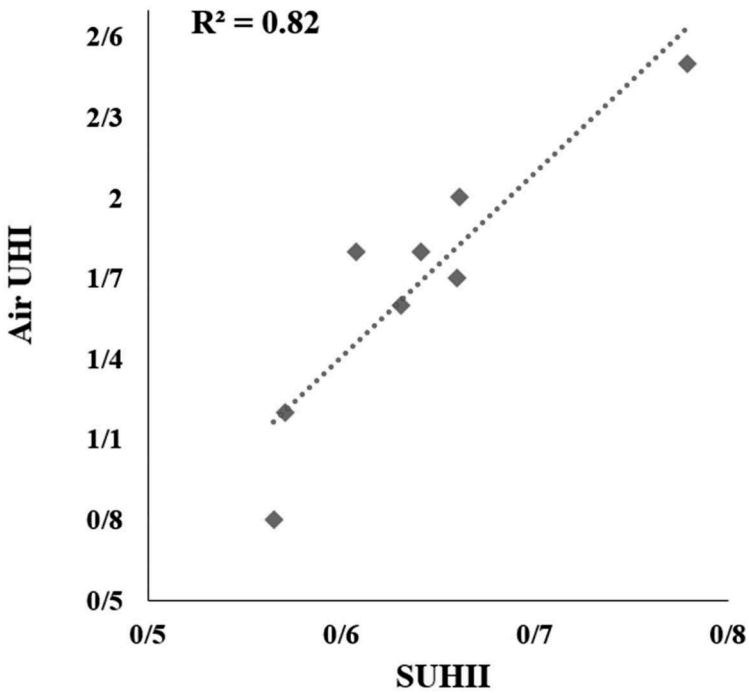


Figure 7. Correlation between air temperature heat island and SUHII.

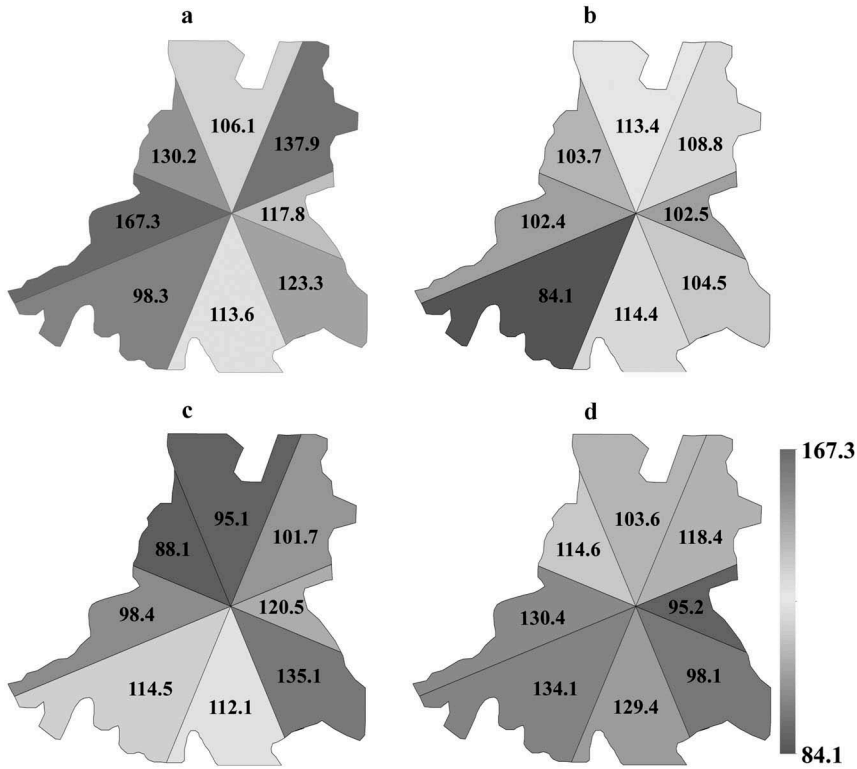


Figure 8. SUHII variation ratio of (a) 1985–1992; (b) 1992–2001; (c) 2001–2008; and (d) 2008–2017 (Percentage).

The SUHII variation ratio for the time period of 1985–1992, 1992–2001, 2001–2008, and 2008–2017 was calculated in different cardinal directions (Table A1 and Figure 8).

The results demonstrated that the SUHII variation changed in different periods and cardinal directions. The W and SW directions had the highest and lowest SUHII variation, respectively. The highest SUHII variation was found in the period from 1985 to 1992, and the lowest in the period of 1992–2001. SUHII variation was reduced in period of 2008–2017 relative to period of 1985–1992.

The values for expected SUHII variation was summarized in Table 5.

Table 5. Values for expected SUHII variation (Percentage).

Period				
Cardinal direction	1985–1992	1992–2001	2001–2008	2008–2017
N	114.9	96.4	100.1	106.8
NW	120.1	100.6	104.5	111.5
W	137.1	114.9	119.3	127.3
SW	118.5	99.3	103.1	110.1
S	129.1	108.2	112.3	119.9
SE	126.7	106.2	110.3	117.7
E	119.9	100.5	104.3	111.3
NE	128.3	107.6	111.7	119.2

The difference between observed and expected SUHII variation was computed by subtracting of the values of these two parameters (Table A2). Table A2 represents the differences in SUHII variation for each direction in each period; in other words, these values represented the degree of deviation of SUHII variations in the spatial and temporal dimensions. Negative values indicated a lower variation, while positive values indicated a variation higher than expected.

4.4.2. Shannon's entropy

Figure 9 shows the result of Shannon's entropy in different time periods and cardinal directions. The result indicated that among all periods, the period of 1985–1992 had the lowest, while the period of 1992–2001 had the highest sprawl value in SUHII variation. The result shows that the SUHII overall observed a high sprawl variation. The value of entropy in most directions was greater than half of $\log_e^m \text{Ln}(m)$ (0.693) (m the number of time periods equal to 4). If the entropy value was less than half of $\log_e^m \text{Ln}(m)$, it could be said that the SUHII was not showing sprawl (Bhatta, Saraswati, and Bandyopadhyay 2010; Dadras et al. 2015). Instead, the SUHII observed a sprawl variation in all directions. Shannon's entropy value was very close to $\log_e^m \text{Ln}(m)$ (1.386) in all directions. High entropy values indicated extreme sprawl SUHII variations.

The overall SUHII sprawl was calculated for specific time periods. The upper limit of the overall sprawl was defined as of $\log_e^m \text{Ln}(n)$ (3.465) (n the number of cardinal directions equal to 8). The overall sprawl was 3.455, which was much higher than half of the value of $\log_e^{n \times m} \text{Ln}(m \times n)$ (1.732) ($m \times n = 32$). Apparently, the SUHII possessed a high sprawl over the period from 1985 to 2017.

4.4.3. Pearson's chi-square

Figure 9 shows the degree-of-freedom in different time periods and different cardinal directions.

The periods of 2001–2008 and 1992–2001 observed the highest and lowest degrees-of-freedom, respectively (Figure 9c). While the SW and W directions possessed the high degree-of-freedom and the NW and S directions detected the low degree-of-freedom in SUHII variation during all periods (Figure 9d). The overall degree-of-freedom of SUHII variation for time interval of 1985–2017 was 50.15. Generally, the degree-of-freedom was extremely high. The high degree-of-freedom reflected the unstable SUHII variation during the study period.

4.4.4. Degree-of-goodness

The results of entropy and degree-of-freedom were inconsistent in some of the cardinal directions and time periods. For example, the period of 2001–2008 showed the lowest amount of Shannon entropy and the highest degree-of-freedom. Similarly, the S cardinal direction detected a high Shannon entropy value, but a lower degree-of-freedom. In this study, the degree-of-goodness was therefore computed to examine consistently the SUHII variation in geographic directions and different periods of time. The computational result of the degree-of-goodness index is shown in Figure 9.

Positive values of degree-of-goodness index indicated the suitable SUHII variation, whereas negative values the unsuitable. The unsuitable SUHII variation means that the

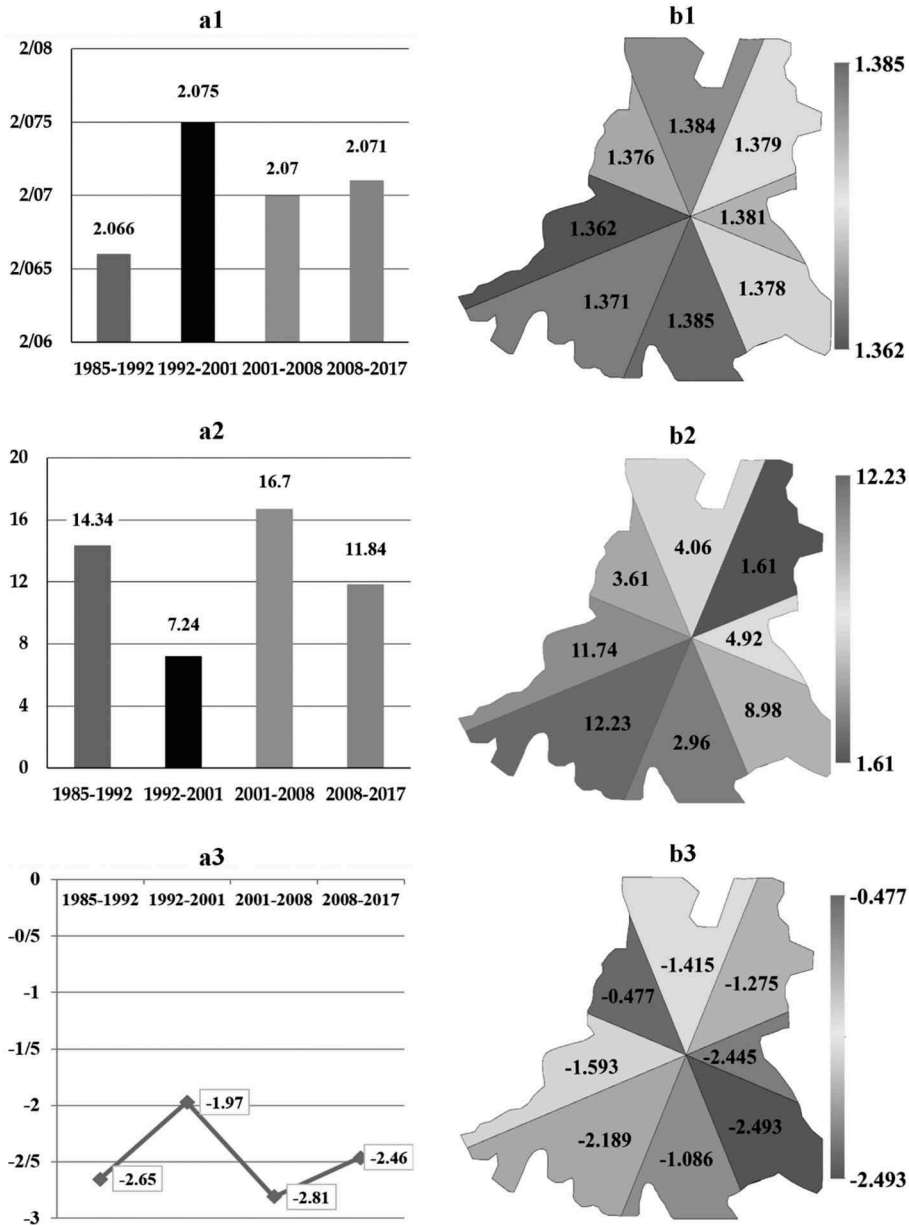


Figure 9. The Shannon's entropy in different time periods (a1) and cardinal directions (b1); the degree-of-freedom in different time periods (a2) and cardinal directions (b2) and the degree-of-goodness of SUHII variation in different time periods (a3) and cardinal directions (b3).

SUHII variation for the study area has not been regular in time periods and different geographic directions, or the SUHII variation has been heterogeneous in spatial and temporal dimensions. The results showed that the SUHII did not have suitable variation

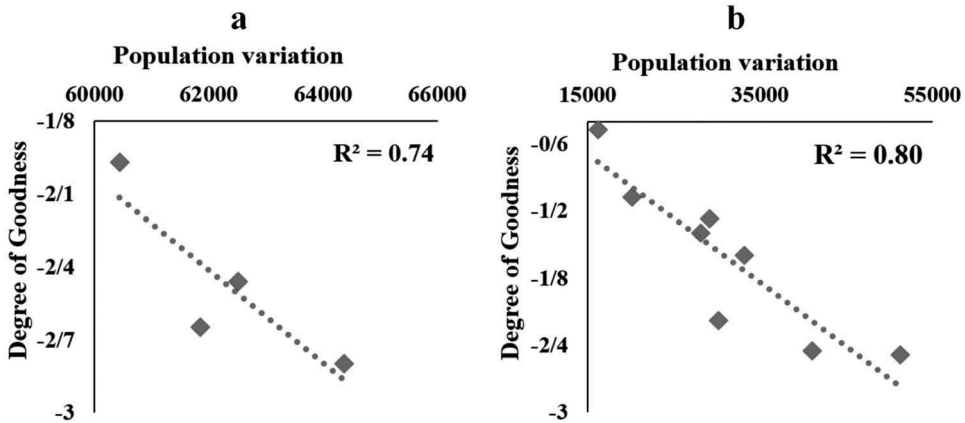


Figure 10. Correlation between the population variation and the degree-of-goodness index in different time periods (a) and cardinal directions (b).

in different periods. In many urban applications, (for example, urban planning) high SUHII variation on different dates or cardinal directions is considered unsuitable. While low SUHII variation are on different dates or cardinal directions is considered suitable. Evaluating this index in different directions also indicated this point, but it was possible to compare periods and different directions with each other. NW and SE directions had the highest and lowest degree-of-goodness of SUHII variation, respectively (Figure 9f). According to this index, the time periods of 1992–2001 and 2001–2008 had the highest and the lowest degree-of-goodness SUHII variation, respectively (Figure 9e)

Figure 10 indicates that there was a strong correlation between the population variation and the degree-of-goodness index in different time periods and cardinal directions.

The overall degree-of-goodness of SUHII variation of the study area was -3.91 , which indicated the overall degree-of-goodness of the SUHII variation was unsuitable. This means that the SUHII variation had not been regular in time periods and different geographic directions, or the SUHII variation had been heterogeneous in spatial and temporal dimensions.

5. Discussion

SUHII index uses the spatial distribution pattern of temperature classes in the region to calculate the SUHII. Many indices for the analysis of the SUHI template only compute one number for a whole study area. It should be noted that due to this disadvantage, in this study, the SUHI was calculated with two global and local (on the scale of different cardinal directions, Figure (6)) strategies. In this study, the SUHII was investigated at the local scale in different geographic directions, while in most previous studies (Firozjaei et al. 2018a; Haashemi et al. 2016; Zhou et al. 2011), SUHII was analyzed at the global scale. To analyze the spatial changes of SUHI, consideration of both spatial and temporal dimensions is vital. In this study, for assessing the SUHII variations trend, degree-of-sprawl and degree-of-freedom indices were utilized. Batta et al. (2010) used chi-square and Shannon entropy for determining the built up growth and sprawl; but the present work showed how this model could be used to analyze the SUHII variation in spatial and temporal dimensions. Since chi-square and Shannon entropy are different measures and one may contradict other in some of the instances (Dadras et al. 2015), an additional index

was employed, referring to as the degree-of-goodness of SUHII variation. In general, degree-of-goodness index can help urban planners evaluate various urban planning practices and programs implemented in different time periods and directions to assess whether the implementation of a particular planning has a positive/negative impact on the SUHII variation during a time period or geographic direction. Research results can provide them with a wealth of useful information. Including:

- (1) The change trend and spatial distribution of different temperature class's information is available for managers to management and decision making.
- (2) The increase of the heat island intensity showed a direct relationship to the population growth and thus, to the rise in the built-up land area. Planners and urban managers need to pay attention to this critical issue.
- (3) It helps managers to understand the SUHI effect and accordingly improve planning practices and programs.
- (4) One of the most important results of the present study is the difference in the SUHII variation trend in different cardinal directions for different time intervals. The indices proposed provide the ability to analyze and compare SUHII variations in spatial (cardinal directions) and temporal (time periods) dimensions. These indices can be easily implemented for other regions and cities in the world.

Finally, whether or not a higher degree-of-goodness is an indication of sustainable development may be debatable since it should be judged with the empirical evidences of sustainability measures, but there is no doubt that a lower degree-of- freedom and lower degree-of-sprawl is the general expectation. Since, the degree-of-goodness is estimated from the products of these two variables, it is a direct measure of the goodness for SUHII variations. Further analytical research would shed some light on the correlation between the degree-of-goodness and sustainable SUHII variations. Although degree-of-goodness cannot be a direct measure of sustainable development, it may be an indicator of sustainable development.

These indices were capable of considering both spatial and temporal dimensions of SUHII simultaneously. Indices used in previous studies analyzed the SUHII variations in spatial and temporal dimensions separately, but did not have the ability to consider both two dimensions simultaneously. Further, in previous studies (Firozjaei et al. 2018a; Haashemi et al. 2016; Panah, Kiavarz Mogaddam, and Karimi Firozjaei 2017), only the decreasing or increasing trend of SUHII variations were evaluated in the whole studied region or time period. The use of the proposed indices, based on statistical relationships, makes it possible to examine the SUHII variations in both spatial and temporal dimensions. The degree-of-goodness was therefore computed to examine consistently the SUHII variation in geographic directions and different periods of time. The results indicated that the spatial pattern of SUHII variations was non-symmetrical.

In order to achieve more practical results, it is suggested in future studies that these indices be implemented in urban districts instead of geographic directions. In addition, applying the results of the study in some predictive models can improve the accuracy of the prediction of SUHII variations for the future. It would be better if some more images in smaller temporal gaps could be considered in the analysis. Needless to say, the reliability of statistical analysis increases with the increase in number of variables in consideration.

6. Conclusions

The UHI is considered as one of the most important urban phenomena, which leads to many negative effects. Analysis of SUHII variations improves the understanding of the effect of urbanization on surface climate and subsequent urban planning. The objective of this study was to present a new strategy based on the Shannon's entropy and Pearson chi-square statistic to study the spatial and temporal variations of the SUHII. The surface urban heat island ratio index was used to calculate the surface urban heat island intensity. Chi-square and entropy indices were used to analyse the SUHI variations. Degree-of-goodness was further been proposed as an additional index to combine the chi-square and entropy as they indicated the spatial and temporal variations of the SUHI. The results revealed that the SUHII increased significantly in Babol city during the period from 1985 to 2017. The SUHII variation varied with geographic direction and time period. The SUHII variation of Babol city showed a high degree-of-freedom, high degree-of-sprawl and negative degree-of-goodness over the time periods. The use of field data, including surface temperature recorded at the weather stations, air temperatures recorded by ground recording devices, topographic and demographic maps, confirmed the performance of the proposed method and the accuracy of the results. These indices were capable of considering both spatial and temporal dimensions of SUHII simultaneously. A limitation of these indices is the level of complexity compared with the previous methods for analysis of SUHII variations. It should be noted that this complexity is entirely for increasing the accuracy and efficiency of the results. Finally, this research provided some important insights into SUHII variations in different geographic directions and time periods, which can be used to optimize urban planning in the future.

Acknowledgements

The authors thank anonymous reviewers for their constructive comments and suggestions which helped to improve the manuscript. The authors would also like to acknowledge NASA/USGS for providing access to Landsat imagery, and the International Relations program of University of Tehran for its support in conducting this research.

Disclosure statement

No potential conflict of interest was reported by the authors.

Funding

This work was supported by the N/A

ORCID

Qihao Weng  <http://orcid.org/0000-0002-2498-0934>

Mohammad Karimi Firozjaei  <http://orcid.org/0000-0002-3060-9162>

Amir Sedighi  <http://orcid.org/0000-0002-4272-2859>

References

- Akbari, H., M. Pomerantz, and H. Taha. 2001. "Cool Surfaces and Shade Trees to Reduce Energy Use and Improve Air Quality in Urban Areas." *Solar Energy* 70 (3): 295–310. doi:10.1016/S0038-092X(00)00089-X.

- Almeida, C. M. D., A. M. V. Monteiro, G. Câmara, B. S. Soares-Filho, G. C. Cerqueira, C. L. Pennachin, and M. Batty. 2005. "GIS and Remote Sensing as Tools for the Simulation of Urban Land-Use Change." *International Journal of Remote Sensing* 26 (4): 759–774. doi:10.1080/01431160512331316865.
- Barsi, J. A., J. R. Schott, S. J. Hook, N. G. Raqueno, B. L. Markham, and R. G. Radocinski. 2014. "Landsat-8 Thermal Infrared Sensor (TIRS) Vicarious Radiometric Calibration." *Remote Sensing* 6 (11): 11607–11626. doi:10.3390/rs61111607.
- Benali, A., A. C. Carvalho, J. P. Nunes, N. Carvalhais, and A. Santos. 2012. "Estimating Air Surface Temperature in Portugal Using MODIS LST Data." *Remote Sensing of Environment* 124: 108–121. doi:10.1016/j.rse.2012.04.024.
- Berk, A., P. Conforti, R. Kennett, T. Perkins, F. Hawes, and J. van den Bosch. 2014. "MODTRAN® 6: A Major Upgrade of the MODTRAN® Radiative Transfer Code." Paper presented at the Hyperspectral Image and Signal Processing: Evolution in Remote Sensing (WHISPERS), 2014 6th Workshop on, Lausanne, Switzerland.
- Bhatta, B. 2009. "Modelling of Urban Growth Boundary Using Geoinformatics." *International Journal of Digital Earth* 2 (4): 359–381. doi:10.1080/17538940902971383.
- Bhatta, B., S. Saraswati, and D. Bandyopadhyay. 2010. "Quantifying the Degree-Of-Freedom, Degree-Of-Sprawl, and Degree-Of-Goodness of Urban Growth from Remote Sensing Data." *Applied Geography* 30 (1): 96–111. doi:10.1016/j.apgeog.2009.08.001.
- Bonham-Carter, G. F. 2014. *Geographic Information Systems for Geoscientists: Modelling with GIS*. 13 vols. New York, NY: Elsevier.
- Cao, L., P. Li, L. Zhang, and T. Chen. 2008. "Remote Sensing Image-Based Analysis of the Relationship between Urban Heat Island and Vegetation Fraction." *The International Archives of the Photogrammetry, Remote Sensing and Spatial Information Sciences* 37: 1379–1384.
- Changnon, S. A., K. E. Kunkel, and B. C. Reinke. 1996. "Impacts and Responses to the 1995 Heat Wave: A Call to Action." *Bulletin of the American Meteorological Society* 77 (7): 1497–1506. doi:10.1175/1520-0477(1996)077<1497:IARTTH>2.0.CO;2.
- Chen, X.-L., H.-M. Zhao, P.-X. Li, and Z.-Y. Yin. 2006. "Remote Sensing Image-Based Analysis of the Relationship between Urban Heat Island and Land Use/Cover Changes." *Remote Sensing of Environment* 104 (2): 133–146. doi:10.1016/j.rse.2005.11.016.
- Cooley, T., G. P. Anderson, G. W. Felde, M. L. Hoke, A. J. Ratkowski, J. H. Chetwynd, J. A. Gardner, S. M. Adler-Golden, M. W. Matthew, and A. Berk. 2002. "FLAASH, a MODTRAN4-based Atmospheric Correction Algorithm, Its Application and Validation." Paper presented at the Geoscience and Remote Sensing Symposium, 2002. IGARSS'02. 2002 IEEE International. doi:10.1044/1059-0889(2002/er01).
- Dadras, M., H. Z. M. Shafri, N. Ahmad, B. Pradhan, and S. Safarpour. 2015. "Spatio-Temporal Analysis of Urban Growth from Remote Sensing Data in Bandar Abbas City, Iran." *The Egyptian Journal of Remote Sensing and Space Science* 18 (1): 35–52. doi:10.1016/j.ejrs.2015.03.005.
- Deng, C., and C. Wu. 2013. "Examining the Impacts of Urban Biophysical Compositions on Surface Urban Heat Island: A Spectral Unmixing and Thermal Mixing Approach." *Remote Sensing of Environment* 131: 262–274. doi:10.1016/j.rse.2012.12.020.
- Ezimand, K., A. A. Kakroodi, and M. Kiavarz. 2018. "The Development of Spectral Indices for Detecting Built-Up Land Areas and Their Relationship with Land-Surface Temperature." *International Journal of Remote Sensing* 1–22, Published online: 03 Jul 2018.
- Firozjaei, M. K., M. Kiavarz, S. K. Alavipanah, T. Lakes, and S. Qureshi. 2018a. "Monitoring and Forecasting Heat Island Intensity through Multi-Temporal Image Analysis and Cellular automata-Markov Chain Modelling: A Case of Babol City, Iran." *Ecological Indicators* 91: 155–170. doi:10.1016/j.ecolind.2018.03.052.
- Firozjaei, M. K., O. Nematollahi, N. Mijani, S. N. Shorabeh, H. K. Firozjaei, and A. Toomanian. 2018b. "An Integrated GIS-based Ordered Weighted Averaging Analysis for Solar Energy Evaluation in Iran: Current Conditions and Future Planning." *Renewable Energy*. doi:10.1016/j.renene.2018.09.090.
- Garcia-Cueto, O. R., E. Jauregui-Ostos, D. Toudert, and D. Tejada-Martinez. 2007. "Detection of the Urban Heat Island in Mexicali, BC, Mexico and Its Relationship with Land Use." *Atmósfera* 20 (2): 111–131.
- Georgescu, M., M. Moustaoui, A. Mahalov, and J. Dudhia. 2011. "An Alternative Explanation of the Semiarid Urban Area 'Oasis Effect'." *Journal of Geophysical Research: Atmospheres* 116: D24. doi:10.1029/2011JD016720.

- Grimm, N. B., S. H. Faeth, N. E. Golubiewski, C. L. Redman, W. Jianguo, X. Bai, and J. M. Briggs. 2008. "Global Change and the Ecology of Cities." *Science* 319 (5864): 756–760. doi:10.1126/science.1150195.
- Guhathakurta, S., and P. Gober. 2007. "The Impact of the Phoenix Urban Heat Island on Residential Water Use." *Journal of the American Planning Association* 73 (3): 317–329. doi:10.1080/01944360708977980.
- Haashemi, S., Q. Weng, A. Darvishi, and S. K. Alavipanah. 2016. "Seasonal Variations of the Surface Urban Heat Island in a Semi-Arid City." *Remote Sensing* 8 (4): 352. doi:10.3390/rs8040352.
- Han-Qiu, X., and C. Ben-Qing. 2004. "Remote Sensing of the Urban Heat Island and Its Changes in Xiamen City of SE China." *Journal of Environmental Sciences* 16 (2): 276–281.
- Ho, H. C., A. Knudby, and W. Huang. 2014. "Estimating Community Health Risks during Extreme Hot Weather Events." Paper presented at the 2014 GSA Annual Meeting in Vancouver, British Columbia.
- Howard, L. 1833. *The Climate of London*. I–III vols. London: Harvey and Dorton.
- Huang, F., W. Zhan, J. Voogt, H. Leiqiu, Z. Wang, J. Quan, J. Weimin, and Z. Guo. 2016. "Temporal Upscaling of Surface Urban Heat Island by Incorporating an Annual Temperature Cycle Model: A Tale of Two Cities." *Remote Sensing of Environment* 186: 1–12. doi:10.1016/j.rse.2016.08.009.
- Imhoff, M. L., P. Zhang, R. E. Wolfe, and L. Bounoua. 2010. "Remote Sensing of the Urban Heat Island Effect across Biomes in the Continental USA." *Remote Sensing of Environment* 114 (3): 504–513. doi:10.1016/j.rse.2009.10.008.
- Jiménez-Muñoz, J. C., and J. A. Sobrino. 2003. "A Generalized Single-Channel Method for Retrieving Land Surface Temperature from Remote Sensing Data." *Journal of Geophysical Research: Atmospheres* 108 (D22). doi:10.1029/2003JD003480.
- Jiménez-Muñoz, J. C., J. A. Sobrino, D. Skoković, C. Mattar, and C. Jordi. 2014. "Land Surface Temperature Retrieval Methods from Landsat-8 Thermal Infrared Sensor Data." *Ieee Geoscience and Remote Sensing Letters* 11 (10): 1840–1843. doi:10.1109/LGRS.2014.2312032.
- Knapp, S., I. Kühn, J. Stolle, and S. Klotz. 2010. "Changes in the Functional Composition of a Central European Urban Flora over Three Centuries." *Perspectives in Plant Ecology, Evolution and Systematics* 12 (3): 235–244. doi:10.1016/j.ppees.2009.11.001.
- Kumar, J. A. V., S. K. Pathan, and R. J. Bhandari. 2007. "Spatio-Temporal Analysis for Monitoring Urban Growth—A Case Study of Indore City." *Journal of the Indian Society of Remote Sensing* 35 (1): 11–20. doi:10.1007/BF02991829.
- Laforteza, R., G. Carrus, G. Sanesi, and C. Davies. 2009. "Benefits and Well-Being Perceived by People Visiting Green Spaces in Periods of Heat Stress." *Urban Forestry & Urban Greening* 8 (2): 97–108. doi:10.1016/j.ufug.2009.02.003.
- Lata, K. M., C. H. S. Rao, V. K. Prasad, K. V. S. Badarianth, and V. Rahgavasamy. 2001. "Measuring Urban Sprawl: A Case Study of Hyderabad." *GIS Development* 5 (12): 26–29.
- Li, J., C. Song, L. Cao, F. Zhu, X. Meng, and W. Jianguo. 2011. "Impacts of Landscape Structure on Surface Urban Heat Islands: A Case Study of Shanghai, China." *Remote Sensing of Environment* 115 (12): 3249–3263. doi:10.1016/j.rse.2011.07.008.
- Li, X., and A. G.-O. Yeh. 2004. "Analyzing Spatial Restructuring of Land Use Patterns in a Fast Growing Region Using Remote Sensing and GIS." *Landscape and Urban Planning* 69 (4): 335–354. doi:10.1016/j.landurbplan.2003.10.033.
- Li, X., L. Wenwen, A. Middel, S. L. Harlan, A. J. Brazel, and B. L. Turner. 2016. "Remote Sensing of the Surface Urban Heat Island and Land Architecture in Phoenix, Arizona: Combined Effects of Land Composition and Configuration and Cadastral–Demographic–Economic Factors." *Remote Sensing of Environment* 174: 233–243. doi:10.1016/j.rse.2015.12.022.
- Liu, L., and Y. Zhang. 2011. "Urban Heat Island Analysis Using the Landsat TM Data and ASTER Data: A Case Study in Hong Kong." *Remote Sensing* 3 (7): 1535–1552. doi:10.3390/rs3071535.
- Lo, C. P., and D. A. Quattrochi. 2003. "Land-Use and Land-Cover Change, Urban Heat Island Phenomenon, and Health Implications." *Photogrammetric Engineering & Remote Sensing* 69 (9): 1053–1063. doi:10.14358/PERS.69.9.1053.
- Mackey, C. W., X. Lee, and R. B. Smith. 2012. "Remotely Sensing the Cooling Effects of City Scale Efforts to Reduce Urban Heat Island." *Building and Environment* 49: 348–358. doi:10.1016/j.buildenv.2011.08.004.
- Moghaddam, M., H. Rezaei, A. Sedighi, S. Fasihi, and M. K. Firozjaei. 2018. "Effect of Environmental Policies in Combating Aeolian Desertification over Sejzy Plain of Iran." *Aeolian Research* 35: 19–28. doi:10.1016/j.aeolia.2018.09.001.

- Moghaddam, M., H. Rezaei, A. Sedighi, and M. A. Fayyazi. 2015. "Applying MNDWI Index and Linear Directional Mean Analysis for Morphological Changes in the Zarriné-Rūd River." *Arabian Journal of Geosciences* 8 (10): 8419–8428. doi:10.1007/s12517-015-1795-6.
- Otukei, J. R., and T. Blaschke. 2010. "Land Cover Change Assessment Using Decision Trees, Support Vector Machines and Maximum Likelihood Classification Algorithms." *International Journal of Applied Earth Observation and Geoinformation* 12: S27–S31. doi:10.1016/j.jag.2009.11.002.
- Panah, S. K., M. Kiavarz Mogaddam, and M. Karimi Firozjaei. 2017. "Monitoring Spatiotemporal Changes of Heat Island in Babol City Due to Land Use Changes." *International Archives of the Photogrammetry, Remote Sensing & Spatial Information Sciences* XLII-4/W4, 2017 Tehran's Joint ISPRS Conferences of GI Research, SMPR and EOEC 2017, 7–10 October 2017, Tehran, Iran.
- Parker, D. E. 2010. "Urban Heat Island Effects on Estimates of Observed Climate Change." *Wiley Interdisciplinary Reviews: Climate Change* 1 (1): 123–133.
- Prihodko, L., and S. N. Goward. 1997. "Estimation of Air Temperature from Remotely Sensed Surface Observations." *Remote Sensing of Environment* 60 (3): 335–346. doi:10.1016/S0034-4257(96)00216-7.
- Qiao, Z., G. Tian, L. Zhang, and X. Xinliang. 2014. "Influences of Urban Expansion on Urban Heat Island in Beijing during 1989–2010." *Advances in Meteorology* 2014. <http://dx.doi.org/10.1155/2014/187169>.
- Qin, Q., N. Zhang, P. Nan, and L. Chai. 2011. "Geothermal Area Detection Using Landsat ETM+ Thermal Infrared Data and Its Mechanistic analysis—A Case Study in Tengchong, China." *International Journal of Applied Earth Observation and Geoinformation* 13 (4): 552–559. doi:10.1016/j.jag.2011.02.005.
- Quan, J., Y. Chen, W. Zhan, J. Wang, J. Voogt, and M. Wang. 2014. "Multi-Temporal Trajectory of the Urban Heat Island Centroid in Beijing, China Based on a Gaussian Volume Model." *Remote Sensing of Environment* 149: 33–46. doi:10.1016/j.rse.2014.03.037.
- Rajasekar, U., and Q. Weng. 2009. "Urban Heat Island Monitoring and Analysis Using A Non-Parametric Model: A Case Study of Indianapolis." *Ispr Journal of Photogrammetry and Remote Sensing* 64 (1): 86–96. doi:10.1016/j.isprsjprs.2008.05.002.
- Rizwan, A. M., L. Y. C. Dennis, and L. I. U. Chunho. 2008. "A Review on the Generation, Determination and Mitigation of Urban Heat Island." *Journal of Environmental Sciences* 20 (1): 120–128. doi:10.1016/S1001-0742(08)60019-4.
- Roth, M., T. R. Oke, and W. J. Emery. 1989. "Satellite-Derived Urban Heat Islands from Three Coastal Cities and the Utilization of Such Data in Urban Climatology." *International Journal of Remote Sensing* 10 (11): 1699–1720. doi:10.1080/01431168908904002.
- Santamouris, M. 2015. "Regulating the Damaged Thermostat of the cities—Status, Impacts and Mitigation Challenges." *Energy and Buildings* 91: 43–56. doi:10.1016/j.enbuild.2015.01.027.
- Schwarz, N., S. Lautenbach, and R. Seppelt. 2011. "Exploring Indicators for Quantifying Surface Urban Heat Islands of European Cities with MODIS Land Surface Temperatures." *Remote Sensing of Environment* 115 (12): 3175–3186. doi:10.1016/j.rse.2011.07.003.
- Shen, H., L. Huang, L. Zhang, W. Penghai, and C. Zeng. 2016. "Long-Term and Fine-Scale Satellite Monitoring of the Urban Heat Island Effect by the Fusion of Multi-Temporal and Multi-Sensor Remote Sensed Data: A 26-Year Case Study of the City of Wuhan in China." *Remote Sensing of Environment* 172: 109–125. doi:10.1016/j.rse.2015.11.005.
- Sobrino, J. A., and N. Raissouni. 2000. "Toward Remote Sensing Methods for Land Cover Dynamic Monitoring: Application to Morocco." *International Journal of Remote Sensing* 21 (2): 353–366. doi:10.1080/014311600210876.
- Sobrino, J. A., J. C. Jiménez-Muñoz, and L. Paolini. 2004. "Land Surface Temperature Retrieval from LANDSAT TM 5." *Remote Sensing of Environment* 90 (4): 434–440. doi:10.1016/j.rse.2004.02.003.
- Sobrino, J. A., J. C. Jiménez-Muñoz, G. Sòria, M. Romaguera, L. Guanter, J. Moreno, A. Plaza, and P. Martínez. 2008. "Land Surface Emissivity Retrieval from Different VNIR and TIR Sensors." *Ieee Transactions on Geoscience and Remote Sensing* 46 (2): 316–327. doi:10.1109/TGRS.2007.904834.
- Srivastava, P. K., T. J. Majumdar, and A. K. Bhattacharya. 2009. "Surface Temperature Estimation in Singhbhum Shear Zone of India Using Landsat-7 ETM+ Thermal Infrared Data." *Advances in Space Research* 43 (10): 1563–1574. doi:10.1016/j.asr.2009.01.023.
- Steenefeld, G. J., S. Koopmans, B. G. Heusinkveld, L. W. A. Van Hove, and A. A. M. Holtslag. 2011. "Quantifying Urban Heat Island Effects and Human Comfort for Cities of Variable Size

- and Urban Morphology in the Netherlands.” *Journal of Geophysical Research: Atmospheres* 116: D20. doi:10.1029/2011JD015988.
- Stone, B. 2008. “Urban Sprawl and Air Quality in Large US Cities.” *Journal of Environmental Management* 86 (4): 688–698. doi:10.1016/j.jenvman.2006.12.034.
- Streutker, D. R. 2002. “A Remote Sensing Study of the Urban Heat Island of Houston, Texas.” *International Journal of Remote Sensing* 23 (13): 2595–2608. doi:10.1080/01431160110115023.
- Sudhira, H. S., T. V. Ramachandra, and K. S. Jagadish. 2004. “Urban Sprawl: Metrics, Dynamics and Modelling Using GIS.” *International Journal of Applied Earth Observation and Geoinformation* 5 (1): 29–39. doi:10.1016/j.jag.2003.08.002.
- Sun, Y., and S. Zhao. 2018. “Spatiotemporal Dynamics of Urban Expansion in 13 Cities across the Jing-Jin-Ji Urban Agglomeration from 1978 to 2015.” *Ecological Indicators* 87: 302–313. doi:10.1016/j.ecolind.2017.12.038.
- Tan, J., Y. Zheng, X. Tang, C. Guo, L. Liping, G. Song, X. Zhen, D. Yuan, A. J. Kalkstein, and L. Furong. 2010. “The Urban Heat Island and Its Impact on Heat Waves and Human Health in Shanghai.” *International Journal of Biometeorology* 54 (1): 75–84. doi:10.1007/s00484-009-0256-x.
- Toller, G. N., A. Isaacman, M. C. S. T. Task Leader, and V. Salomonson. 2003. “MODIS Level 1B Product User’s Guide.” *Signature (Ramsey, N.J.)*.
- Tran, H., D. Uchihama, S. Ochi, and Y. Yasuoka. 2006. “Assessment with Satellite Data of the Urban Heat Island Effects in Asian Mega Cities.” *International Journal of Applied Earth Observation and Geoinformation* 8 (1): 34–48. doi:10.1016/j.jag.2005.05.003.
- Tucker, C. J. 1979. “Red and Photographic Infrared Linear Combinations for Monitoring Vegetation.” *Remote Sensing of Environment* 8 (2): 127–150. doi:10.1016/0034-4257(79)90013-0.
- Vancutsem, C., P. Ceccato, T. Dinku, and S. J. Connor. 2010. “Evaluation of MODIS Land Surface Temperature Data to Estimate Air Temperature in Different Ecosystems over Africa.” *Remote Sensing of Environment* 114 (2): 449–465. doi:10.1016/j.rse.2009.10.002.
- Voogt, J. A., and T. R. Oke. 2003. “Thermal Remote Sensing of Urban Climates.” *Remote Sensing of Environment* 86 (3): 370–384. doi:10.1016/S0034-4257(03)00079-8.
- Walawender, J. P., M. Szymanowski, M. J. Hajto, and A. Bokwa. 2014. “Land Surface Temperature Patterns in the Urban Agglomeration of Krakow (Poland) Derived from Landsat-7/ETM+ Data.” *Pure and Applied Geophysics* 171 (6): 913–940. doi:10.1007/s00024-013-0685-7.
- Weng, Q. 2009. “Thermal Infrared Remote Sensing for Urban Climate and Environmental Studies: Methods, Applications, and Trends.” *Isprs Journal of Photogrammetry and Remote Sensing* 64 (4): 335–344. doi:10.1016/j.isprs.2009.03.007.
- Weng, Q., M. K. Firozjaei, M. Kiavarz, S. K. Alavipanah, and S. Hamzeh. 2019. “Normalizing Land Surface Temperature for Environmental Parameters in Mountainous and Urban Areas of a Cold Semi-Arid Climate.” *Science of the Total Environment* 650: 515–529. doi:10.1016/j.scitotenv.2018.09.027.
- Weng, Q., U. Rajasekar, and H. Xuefei. 2011. “Modeling Urban Heat Islands and Their Relationship with Impervious Surface and Vegetation Abundance by Using ASTER Images.” *Ieee Transactions on Geoscience and Remote Sensing* 49 (10): 4080–4089. doi:10.1109/TGRS.2011.2128874.
- Xu, H. Q., and B. Q. Chen. 2003. “An Image Processing Technique for the Study of Urban Heat Island Changes Using Different Seasonal Remote Sensing Data.” *Remote Sensing Technology and Application* 18 (3): 129–133.
- Yeh, A. G.-O., and X. Li. 2001. “Measurement and Monitoring of Urban Sprawl in a Rapidly Growing Region Using Entropy.” *Photogrammetric Engineering and Remote Sensing* 67 (1): 83–90.
- Yuan, F., and M. E. Bauer. 2007. “Comparison of Impervious Surface Area and Normalized Difference Vegetation Index as Indicators of Surface Urban Heat Island Effects in Landsat Imagery.” *Remote Sensing of Environment* 106 (3): 375–386. doi:10.1016/j.rse.2006.09.003.
- Zhang, J., and Y. Wang. 2008. “Study of the Relationships between the Spatial Extent of Surface Urban Heat Islands and Urban Characteristic Factors Based on Landsat ETM+ Data.” *Sensors* 8 (11): 7453–7468. doi:10.3390/s8117453.
- Zhou, B., D. Rybski, and J. P. Kropp. 2017. “The Role of City Size and Urban Form in the Surface Urban Heat Island.” *Scientific Reports* 7 (1): 4791. doi:10.1038/s41598-017-04242-2.
- Zhou, J., Y. Chen, J. Wang, and W. Zhan. 2011. “Maximum Nighttime Urban Heat Island (UHI) Intensity Simulation by Integrating Remotely Sensed Data and Meteorological Observations.” *IEEE Journal of Selected Topics in Applied Earth Observations and Remote Sensing* 4 (1): 138–146. doi:10.1109/JSTARS.2010.2070871.

Appendix 1

Table A1. SUHII variation ratio of (a) 1985–1992; (b) 1992–2001; (c) 2001–2008; and (d) 2008–2017 (Percentage).

period Cardinal direction	<i>1985–1992</i>	<i>1992–2001</i>	<i>2001–2008</i>	<i>2008–2017</i>
N	106.0	113.4	95.1	103.6
NW	130.2	103.7	88.1	114.6
W	167.3	102.4	98.5	130.4
SW	98.3	84.1	114.5	134.1
S	113.6	114.4	112.0	129.4
SE	123.3	104.5	135.1	98.1
E	113.6	102.5	120.5	95.2
NE	137.9	108.8	101.7	118.4

Table A2. Difference between the observed and expected SUHII variation ratio (Percentage).

period Cardinal direction	<i>1985–1992</i>	<i>1992–2001</i>	<i>2001–2008</i>	<i>2008–2017</i>
N	-8.9	17.1	-4.9	-3.1
NE	10.2	3.1	-16.3	3.1
E	30.2	-12.5	-20.8	3.1
SE	-20.1	-15.2	11.4	23.9
S	-15.4	6.2	-0.3	9.5
SW	-3.4	-1.7	24.8	-19.6
W	-2.1	1.9	16.2	-16.1
NW	9.5	1.2	-9.9	-0.8